

# Precipitation, temperature, and moisture transport variations associated with two distinct ENSO flavors during 1979–2014

Guojun Gu<sup>1</sup>  · Robert F. Adler<sup>1</sup>

Received: 15 July 2016 / Accepted: 16 November 2016 / Published online: 22 November 2016  
© Springer-Verlag Berlin Heidelberg 2016

**Abstract** Interannual precipitation and temperature variations during 1979–2014 are investigated by examining the effects of two distinct flavors of the El Niño–Southern Oscillation (ENSO), i.e., the tropical eastern Pacific (EP) and central Pacific (CP) ENSO events. Satellite- and ground-based observations with global coverage are applied including the monthly precipitation data from the Global Precipitation Climatology Project (GPCP) and surface temperature anomalies from the NASA-GISS surface temperature anomaly analysis. Related variations in other water-cycle components including atmospheric moisture transport are also examined by using the outputs from the NASA-Modern Era Retrospective-analysis for Research and Applications (MERRA). While the second leading mode from an EOF analysis of sea surface temperature (SST) anomalies between 30°N and 30°S is dominated by interdecadal-scale variability that is not a focus of this study, the first and third leading modes represent well the EP and CP events, respectively. The corresponding principal components (PC1 and PC3) are then

applied as indices to estimate the influences of the two ENSO flavors on various physical components through linear regression. Because of their distinct SST configurations in the tropical Pacific, the two ENSO flavors manifest different spatial features of precipitation anomalies as shown in past studies. Differences can also be readily seen in satellite-retrieved tropospheric layered temperatures and oceanic columnar water vapor content. General agreements between observations and MERRA outputs can be obtained as judged by consistent respective anomalies corresponding to the two ENSO flavors, suggesting that MERRA could provide an accurate account of variations on the interannual time scale. Interannual variations in MERRA vertically integrated moisture transport (VIMT) are further examined to explore possible relations between precipitation and tropospheric moisture transport corresponding to the two flavors during two contrasting seasons: December–March (DJFM) and June–September (JJAS). Anomalies of zonal moisture transport in the deep tropics following the variations in the Pacific Walker Circulation are distinctly different for two ENSO flavors and also manifest evident seasonal variations for each flavor. Differences in the zonal mean VIMT (both zonal and meridional components) are also evident between the two flavors, consistent with the differences in zonal mean precipitation anomalies from both GPCP and MERRA. Furthermore, the ENSO flavors are associated with distinct precipitation anomaly patterns over various land areas, which can be further traced to the differences in their associated VIMT anomalies, particularly during DJFM when the warm ENSO events usually reach their mature phase.

---

This paper is a contribution to the special collection on ENSO Diversity. The special collection aims at improving understanding of the origin, evolution, and impacts of ENSO events that differ in amplitude and spatial patterns, in both observational and modeling contexts, and in the current as well as future climate scenarios. This special collection is coordinated by Antonietta Capotondi, Eric Guilyardi, Ben Kirtman and Sang-Wook Yeh.

---

✉ Guojun Gu  
ggu@umd.edu

<sup>1</sup> Earth System Science Interdisciplinary Center, University of Maryland, 5825 University Research Court, Suite 4001, College Park, MD 20740, USA

**Keywords** ENSO flavors · Precipitation variations · Atmospheric moisture transport

## 1 Introduction

The El Niño-Southern Oscillation (ENSO) is a dominant physical mode on the interannual time scale, which can effectively induce precipitation anomalies in the tropics and further extend its influence to the mid-high latitudes of both hemispheres (e.g., Ropelewski and Halpert 1987; Kiladis and Diaz 1989; Dai and Wigley 2000; Curtis and Adler 2003). Two distinct ENSO flavors have been emphasized during the past decade (e.g., Larkin and Harrison 2005; Ashok et al. 2007; Kao and Yu 2009; Kug et al. 2009; Capotondi et al. 2015), though it is still a debate whether they belong to two different categories or just manifest distinct aspects of one phenomenon (e.g., Takahashi et al. 2011; Mayer et al. 2013). The conventional, canonical warm ENSO events are usually observed with their maximum warm zone in the tropical eastern Pacific (EP), while the so-called “Dateline El Niño”, or El Niño Modoki events are often seen with their peak of warming in the tropical central Pacific (CP) (e.g., Larkin and Harrison 2005; Ashok et al. 2007). Because of different spatial structures of sea surface temperature (SST) and accompanying deep convection and precipitation anomalies in the tropical Pacific, the two ENSO flavors, i.e., the EP and CP El Niño, in general correspond to their own unique variation features in the Pacific Walker Circulation (e.g., Ashok et al. 2007; Weng et al. 2007, 2009). Differences in their impacts on precipitation, temperature, and large-scale circulations have been discovered as well in the pan-Pacific basin including East Asia, North America, and Australia, etc. (e.g., Larkin and Harrison 2005; Weng et al. 2007, 2009; Zhang et al. 2014), and in the Indian Ocean and North Atlantic (e.g., Zhang et al. 1997; Graf and Zanchettin 2012). It is shown that the two distinct ENSO flavors may even differently influence the Pacific typhoon/hurricane activities (e.g., Hong et al. 2011; Kim et al. 2011). A closer connection between CP El Niño and climate variations in the North Atlantic/Europe sector has also been suggested (Graf and Zanchettin 2012). Nevertheless, few studies have been directly focused on variations in the global hydrological cycle associated with these two ENSO flavors. In particular, detailed mechanisms of how differently they may influence a variety of the hydrological-cycle components across the world specifically including precipitation and atmospheric moisture transport have not been fully explored.

Therefore, our primary objectives here are to pursue a detailed examination of precipitation and temperature variations associated with the two distinct ENSO flavors during the satellite (1979–2014) era using both satellite and station based observations and a reanalysis product (NASA/MERRA outputs), and then to further investigate related variations in tropospheric moisture transport likely following and/or feeding the variations/changes in precipitation,

the large-scale circulations, and atmospheric thermodynamic states. This can also result in an assessment of the accuracy of the NASA/MERRA water cycle outputs on the interannual time scale.

The paper is organized as follows: Sect. 2 provides a brief introduction of the observations and NASA/MERRA reanalysis product applied in this study. Results and discussions are presented in Sect. 3. Summary and concluding remarks are given in Sect. 4.

## 2 Data sets and methodology

The monthly precipitation data from the Global Precipitation Climatology Project (GPCP) product (Version 2.3) are applied in this study. This is a community-based analysis of global precipitation under the auspices of the World Climate Research Program (WCRP). Archived on a global  $2.5^\circ \times 2.5^\circ$  grid, the data set covers the entire post-1979 period and is produced by merging a variety of data sources, including passive microwave-based rainfall retrievals from the Special Sensor Microwave/Imager (SSM/I) and the Special Sensor Microwave Imager Sounder (SSMIS), infrared (IR) rainfall estimates from geostationary and polar-orbiting satellites, and surface rain gauges. The combination procedures are designed to take advantage of the strengths of individual inputs, specifically in terms of bias reduction (Adler et al. 2003; Huffman et al. 2009).

The NASA-GISS surface temperature anomaly field (1880–present) is applied to examine temperature variations/changes over global land and ocean (Hansen et al. 1999). The product is archived on a global  $2^\circ \times 2^\circ$  grid and re-gridded to the GPCP grids. The data with the 1200-km smoothing level are used here. For extracting SST indices representing interannual variations from tropical ocean ( $30^\circ\text{N}$ – $30^\circ\text{S}$ ; see below), the NOAA Extended Reconstructed Sea Surface Temperature (ERSST) data set (Version 4) is also used (Xue et al. 2003; Smith et al. 2008).

Data from two atmospheric temperature layers derived from the microwave sounding units (MSU) and the advanced microwave sounding units (AMSU) are used to describe the thermal states of tropospheric atmosphere, which are the deep-layered temperatures for the lower troposphere (TLT) and the mid-troposphere (TMT). They are the Version 3.3 products from remote sensing systems (RSS). Archived on the  $2.5^\circ \times 2.5^\circ$  grid, the products last from 1979 to the present. The Version-7 monthly RSS-SSM/I columnar water vapor (CWV) products are also used to examine variations in oceanic total precipitable water for the period of 1988–2014. The data are merged from several intercalibrated satellite retrievals (Wentz 1997) and have been applied in past studies (e.g., Gu and Adler 2013).

Several components from the NASA-Modern Era Retrospective-analysis for Research and Applications (MERRA) are applied (Rienecker et al. 2011). In particular, monthly precipitation, atmospheric temperatures at 850 and 500 hPa, and vertically integrated atmospheric water vapor are first assessed by comparing their anomalies associated with the two distinct ENSO flavors with respective ones derived from the satellite-based observations. Monthly vertically integrated moisture transport (VIMT) from MERRA is then used to quantify tropospheric water vapor transport variations on the interannual time scale:

$$VIMT = \int_{p_s}^0 q \vec{V} \frac{dp}{g},$$

here  $q$  is the specific humidity,  $\vec{V}$  the horizontal wind vector, and  $p_s$  the surface pressure. Two related water-cycle variables, columnar atmospheric moisture convergence and moisture transport potential function ( $\varphi$ ), are further derived from VIMT at global grids (e.g., Sohn et al. 2004):

$$\nabla^2 \varphi = -\nabla \cdot \int_{p_s}^0 q \vec{V} \frac{dp}{g}.$$

In general, total columnar moisture convergence is balanced by the difference between precipitation (P) and surface evaporation/evapotranspiration (E) over a relatively

long period since the temporal tendency of total precipitable water ( $\frac{\partial W}{\partial t}$ ) is small (e.g., Sohn et al. 2004; Trenberth et al. 2011), i.e.,

$$-\nabla \cdot \int_{p_s}^0 q \vec{V} \frac{dp}{g} \approx P - E.$$

### 3 Results

An EOF analysis of monthly SST anomalies from ERSST v4 between 30°N and 30°S is made for the period of 1979–2014. The three leading EOFs and corresponding principal components are depicted in Figs. 1 and 2, respectively. Based on the criterion suggested in North et al. (1982), they are well separated from each other. Interannual variations tend to dominate the first and third modes (Fig. 2a, c). In particular, PC1 is highly correlated with both Nino3.4 and Nino3, while PC3 is significantly correlated with two other indices often used to represent those ENSO events with their maximum warm/cold zone in the tropical central Pacific, i.e., the El Niño Modoki index (EMI; Ashok et al. 2007) and the Trans-Niño index (TNI; Trenberth and Stepaniak 2001). Given their distinct configurations of SST anomalies in the tropical Pacific, the two flavors of ENSO phenomena represented by the standardized PC1 and PC3, respectively, are then examined by exploring and comparing their respective global precipitation and temperature anomalies.

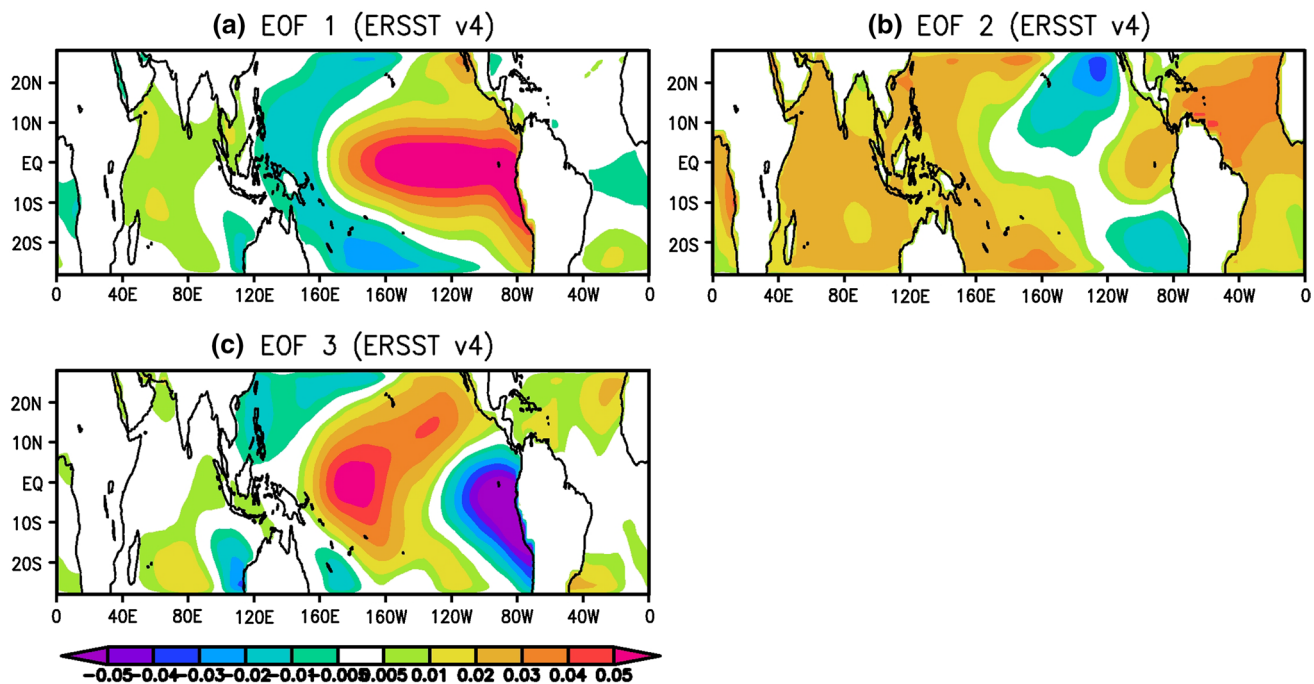
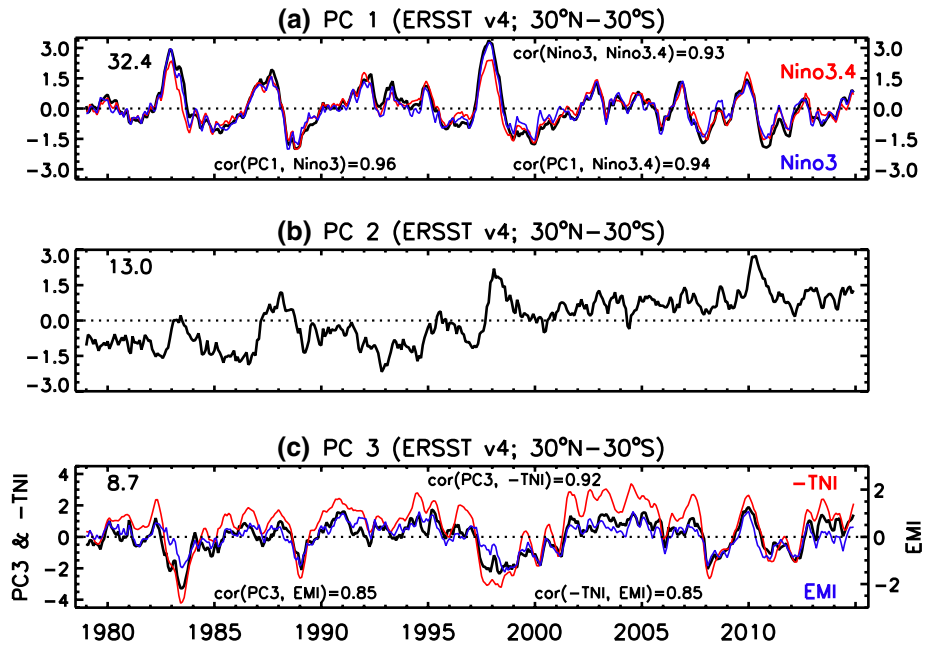


**Fig. 1** The three leading EOF modes of NOAA/ERSST v4 SST monthly anomalies between 30°N and 30°S during 1979–2014

**Fig. 2** The three leading principal components of NOAA/ERSST v4 SST monthly anomalies between 30°N and 30°S during 1979–2014. Also shown are the percentages of variances accounted for by these three modes. For comparison, two ENSO indices, Nino 3.4 (red) and Nino 3 (blue), and are depicted in (a), and two other ENSO indices, TNI (red) and EMI (blue), are shown in (c). Linear correlations between these indices are estimated as well. Also shown are the percentages of variance accounted for by three SST modes



The second EOF mode primarily manifests an evident decadal shift around 1998, in addition to high-frequency components (Figs. 1b, 2b). This decadal shift might mostly be due to the recent phase change of the Pacific Decadal Oscillation (PDO) (e.g., Burgman et al. 2008; Gu and Adler 2013), which has been suggested as the primary cause for the recent global mean temperature hiatus (e.g., Trenberth and Fasullo 2013; Gu and Adler 2013). It is also noted that the upward trend in PC2 might confirm the effect of the anthropogenic radiative forcings during the past more than three decades (e.g., Gu et al. 2016). Several recent studies have explored this mode (e.g., Gu and Adler 2013; Gu et al. 2016). In this study, we will thus only focus on the first and third modes.

### 3.1 Observed precipitation and temperature anomalies associated with two distinct ENSO flavors and a comparison with MERRA

The two ENSO flavors related temperature variations are first examined by regressing GISS temperature anomalies against the standardized PC1 and PC3, respectively (Fig. 3a, b). Spatial features of temperature anomalies in the tropics for two ENSO flavors are similar respectively to the first and third EOFs (Fig. 1), showing their distinct tropical SST configurations. In addition to the differences in the tropics, temperature anomalies corresponding to these two modes are significantly different in the mid-high latitudes of both hemispheres. PC1 related negative anomalies occupy the Northern Hemisphere (NH) extratropics except over the northwestern portion of North America and part of West Europe. For

PC3, positive anomalies are seen over most of the regions north of about 60°N except over part of North America (east of about 100°W), and a band of weak negative anomalies appears between 40 and 60°N within the interior Eurasian continent. Also, PC3 tends to be associated with a tri-polar anomaly pattern in the North Atlantic basin, agreeing with the mechanism on the effect of CP ENSO events on the North Atlantic Oscillation (NAO) (e.g., Graf and Zanchettin 2012). In the southern hemisphere (SH) mid-high latitudes, temperature responses to PC1 and PC3 are also different, especially south of about 50°S. Tropospheric temperature variations associated with these two distinct ENSO flavors are also examined by regressing the MSU/AMSU TLT and TMT anomalies against the standardized PC1 and PC3, respectively (Fig. 3c–f). For PC1, positive anomalies roughly cover the entire deep tropical band (roughly 20°N–20°S) for both TLT and TMT with the most intense anomalies in the Pacific manifesting a dumb-bell-shaped pattern (e.g., Yulaeva and Wallace 1994; Trenberth and Smith 2009). Negative anomalies appear in the subtropics/extratropics of both hemispheres, showing certain zonal and interhemispheric symmetries (e.g., Robinson 2002; Seager et al. 2003). Nevertheless, over part of North America (north of about 40°N) and along the latitudinal band of 60–80°S especially east of the Ross Sea, positive anomalies are seen for both TLT and TMT. For PC3, although positive anomalies appear in the deep tropics as well and manifest a similar dumb-bell-shaped pattern, they are generally localized in the tropical Pacific. PC3 related anomalies can also be seen in the mid-high latitudes, however they manifest different spatial distributions from

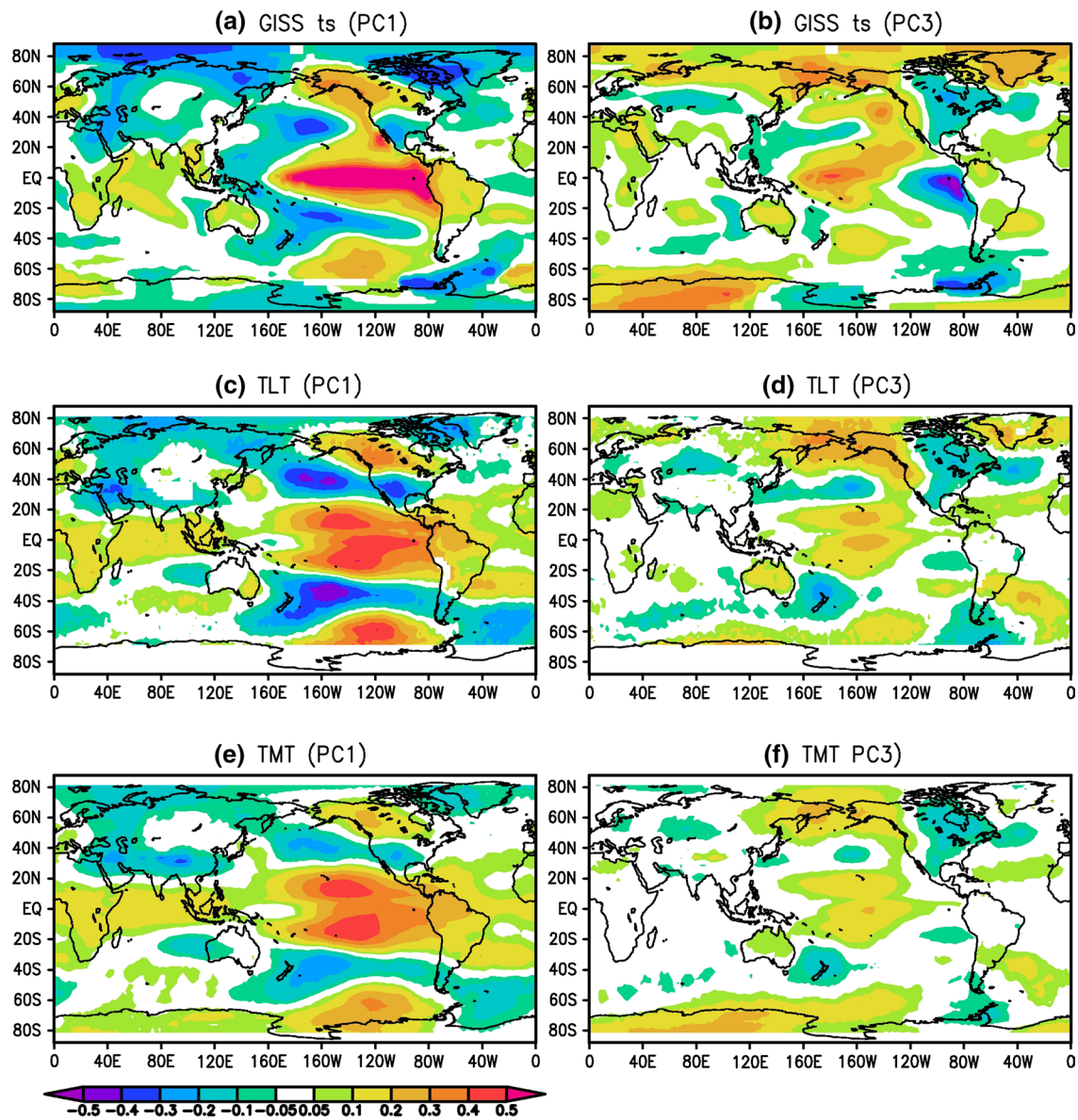


**Fig. 3** Regression maps of GISS ts (a, b), and RSS V3.3 MSU/AMSU TLT (c, d) and TMT (e, f) anomalies (K) onto the standardized PC1 (a, c, e) and PC3 (b, d, f)

and are weaker than PC1 related anomalies. In general, the tropospheric temperature anomalies (TLT and TMT) tend to follow respective surface temperature anomalies for both PC1 and PC3, specifically beyond the deep tropics.

PC1 and PC3 related GPCP monthly precipitation anomalies are illustrated in Fig. 4a, b, respectively. Spatial features of PC1-related precipitation anomalies are consistent with those based on either Nino 3.4 or Nino 3 (e.g., Dai and Wigley 2000; Curtis and Adler 2003), showing the impact of conventional, canonical ENSO events. Positive precipitation anomalies cover the entire tropical central-eastern Pacific with a peak near the dateline and an extension into

the SH subtropics (Fig. 4a), while negative anomalies are seen in the tropical western Pacific with extensions into the subtropics of both hemispheres. PC3 related precipitation anomalies (CP ENSO events) are relatively weak and the zone of maximum positive anomalies shifts farther west (near about 140°E) covering a large portion of the tropical western Pacific (Fig. 4b); East of about 180°W, a band of negative precipitation anomalies occupies the equatorial region with a narrow band of positive anomalies north of it, indicating a northward shift of the climatological ITCZ (e.g., Ashok et al. 2007; Mayer et al. 2013), in contrast to the southward shift of the ITCZ associated with PC1 (EP ENSO events) (Fig. 4a). In the Indian Ocean and Atlantic,

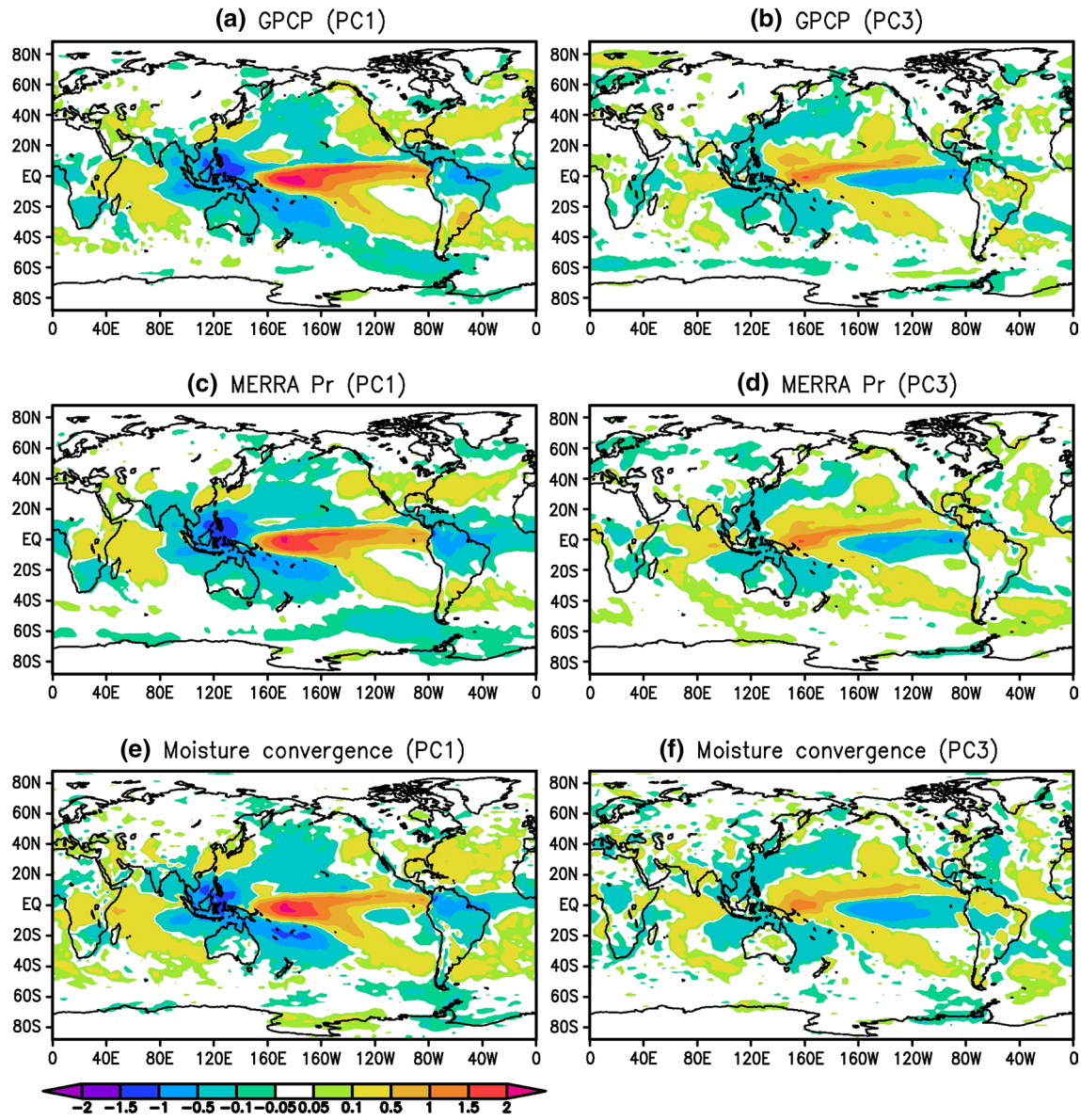


**Fig. 4** Regression maps of GPCP (a, b) and MERRA (c, d) monthly precipitation anomalies ( $\text{mm day}^{-1}$ ), and convergence anomalies ( $\text{mm day}^{-1}$ ) of vertically integrated moisture transport (e, f) onto the standardized PC1 (a, c, e) and PC3 (b, d, f)

the PC3-related precipitation anomalies are also much weaker than those associated with PC1.

Figure 5a, b illustrates the regression of SSM/I oceanic CWV against PC1 and PC3, respectively. Spatial features of CWV anomalies generally follow those of respective precipitation anomalies in particular in the Pacific basin and Indian Ocean, confirming a close correspondence between precipitation and CWV at least on the interannual time scale.

Regressions of MERRA precipitation and columnar water vapor anomalies against the standardized PC1 and PC3 are also estimated, respectively (Figs. 4c, d, 5c, d). Compared to GPCP, similar features can readily be seen

in MERRA precipitation with regard to respective anomalies for both ENSO flavors. Furthermore, MERRA CWV anomalies related to both PC1 and PC3 have similar spatial distributions to the respective ones derived from satellite-based observations. Spatial structures of total moisture convergence anomalies ( $\approx P - E$ , for  $\frac{\partial W}{\partial t} \sim 0$ ) estimated from MERRA VIMT related to PC1 and PC3 are also consistent with their respective ones in GPCP and MERRA precipitation (Fig. 3e, f), likely confirming the high correspondence between the variations in precipitation and tropospheric moisture convergence at least on the interannual time scale. MERRA temperature anomalies at 850 (T850) and 500 hPa (T500) associated with two ENSO flavors are

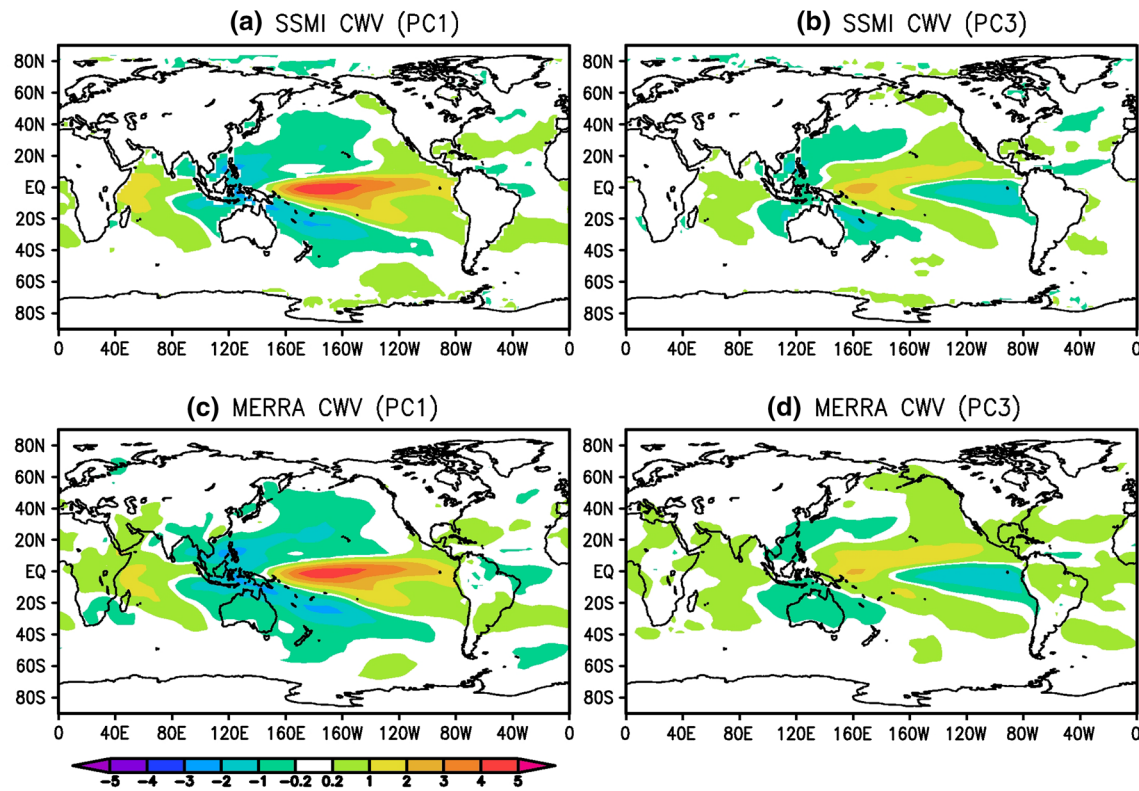


**Fig. 5** Regression maps of (a, b) SSM/I (1988–2014) and (c, d) MERRA CWV (1979–2014) anomalies (mm) onto the standardized PC1 (a, c) and PC3 (b, d)

also estimated (not shown), and further compared to the respective ones from TLT and TMT. Similar spatial structures of anomalies can be found between T850 and TLT, and between T500 and TMT. Therefore, MERRA outputs have high fidelity in describing variations on the interannual time scale as suggested in past studies (e.g., Robertson et al. 2011, 2014). Hence, in the following section, atmospheric moisture transport components from MERRA are applied to further examine and compare the two ENSO flavors related precipitation anomalies and associated large-scale atmospheric moisture transport.

### 3.2 Precipitation, temperature, and large-scale moisture transport anomalies for the two ENSO flavors during two contrasting seasons

To further explore precipitation variations and associated atmospheric moisture transport anomalies corresponding to the two ENSO flavors and their likely seasonality, seasonal mean PC1 and PC3 of these qualities are computed for boreal winter [December–January–February–March (DJFM)] and summer [June–July–August–September (JJAS)] (Fig. 6), respectively. Regressions of seasonal mean GPCP precipitation and GISS temperature anomalies, and MERRA VIMT anomalies are then estimated (Figs. 7, 8).

Spatial structures of precipitation, temperature, and VIMT anomalies are distinctly different between two ENSO flavors within both seasons as expected. For each ENSO flavor seasonal differences are evident as well. During DJFM, PC1 related precipitation and temperature anomalies are generally consistent with those derived for the whole year, confirming that the EP events usually peak in boreal winter (e.g., Trenberth et al. 1998; Trenberth and Stepaniak 2001). During JJAS, PC1 related precipitation anomalies become in general weak in the tropics and the NH subtropics and extratropics (Fig. 7c); south of the equator, positive anomalies along the SPCZ also become weak, but anomalies tend to be stronger and cover a relatively larger area south of about 20°S. VIMT anomalies show strong seasonality as well for PC1 (vectors in Fig. 7a, c), generally in agreement with the seasonal differences in precipitation and temperature anomalies. Intense zonal variations in VIMT appear in both the tropical Pacific and Indian Ocean during DJFM, while the anomalies become much weaker and even hardly discernible in the Indian Ocean during JJAS. In the NH mid-high latitudes, significant southwesterly moisture transport anomalies during DJFM can be seen along/just off the east coast of the Asian continent and in the North Pacific, accompanying positive precipitation anomalies. In the North Pacific, a cyclonic

**Fig. 6** The first (**a**) and third (**b**) leading principal components of NOAA/ERSST v4 SST monthly anomalies between  $30^{\circ}\text{N}$  and  $30^{\circ}\text{S}$  during boreal winter [December–January–February–March (DJFM), black] and summer [June–July–August–September (JJAS), red] season

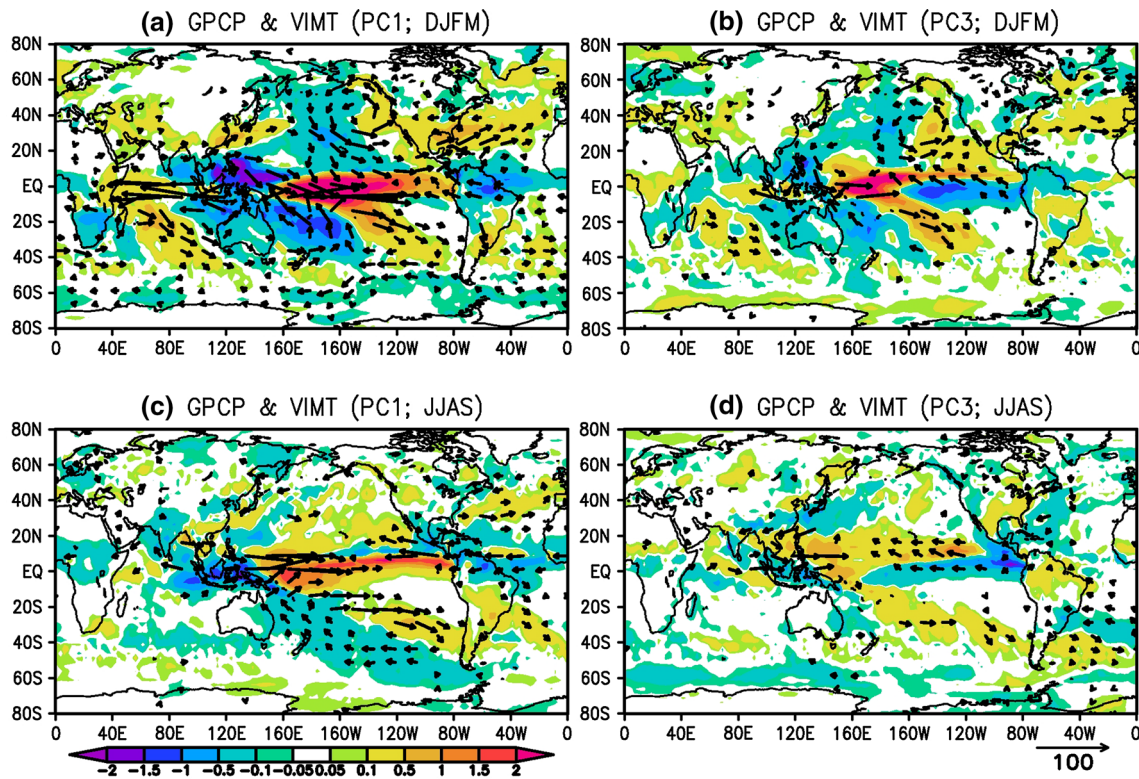
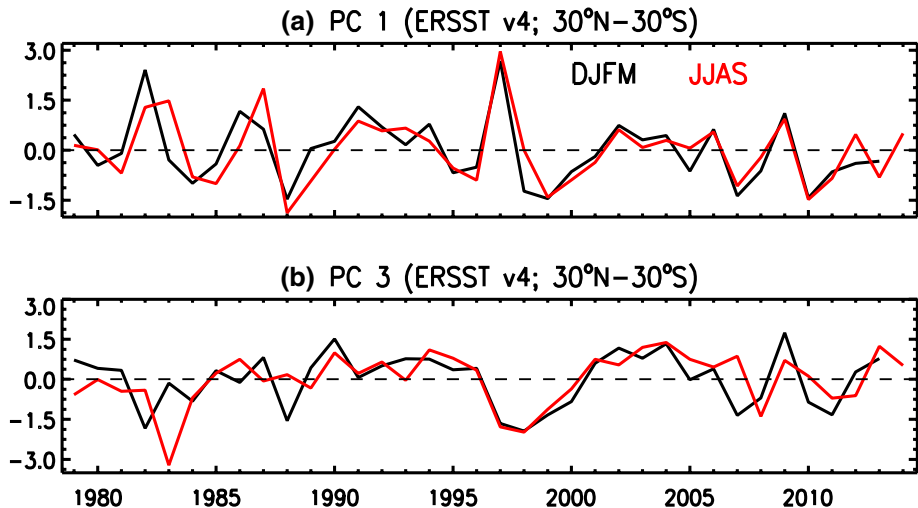


**Fig. 7** GPCP precipitation anomalies ( $\text{mm day}^{-1}$ ; color shades) and vertically integrated moisture transport (VIMT;  $\text{kg m}^{-1} \text{s}^{-1}$ ; vectors) anomalies regressed onto the standardized PC1 (**a**, **c**) and PC3 (**b**, **d**)

during DJFM (**a**, **b**) and JJAS (**c**, **d**), respectively. VIMT vectors are shown only if at least one of their components is at the 90% significance level

anomaly center is seen during DJFM with positive (negative) precipitation anomalies occurring in its northeastern (southwestern) portion. However, VIMT anomalies become much weaker or even indiscernible in these regions during JJAS.

Spatial structures of PC3 related precipitation anomalies are similar in the tropical region in the two seasons,

although anomalies are also weaker during JJAS than during DJFM (Fig. 7b, d). Nevertheless, positive anomalies during JJAS can extend farther westward to cover most of the northern portion of the Maritime Continent and Southeast Asia. VIMT anomalies also manifest strong seasonality following the seasonal differences in precipitation anomalies. In particular, VIMT anomalies in the NH subtropics

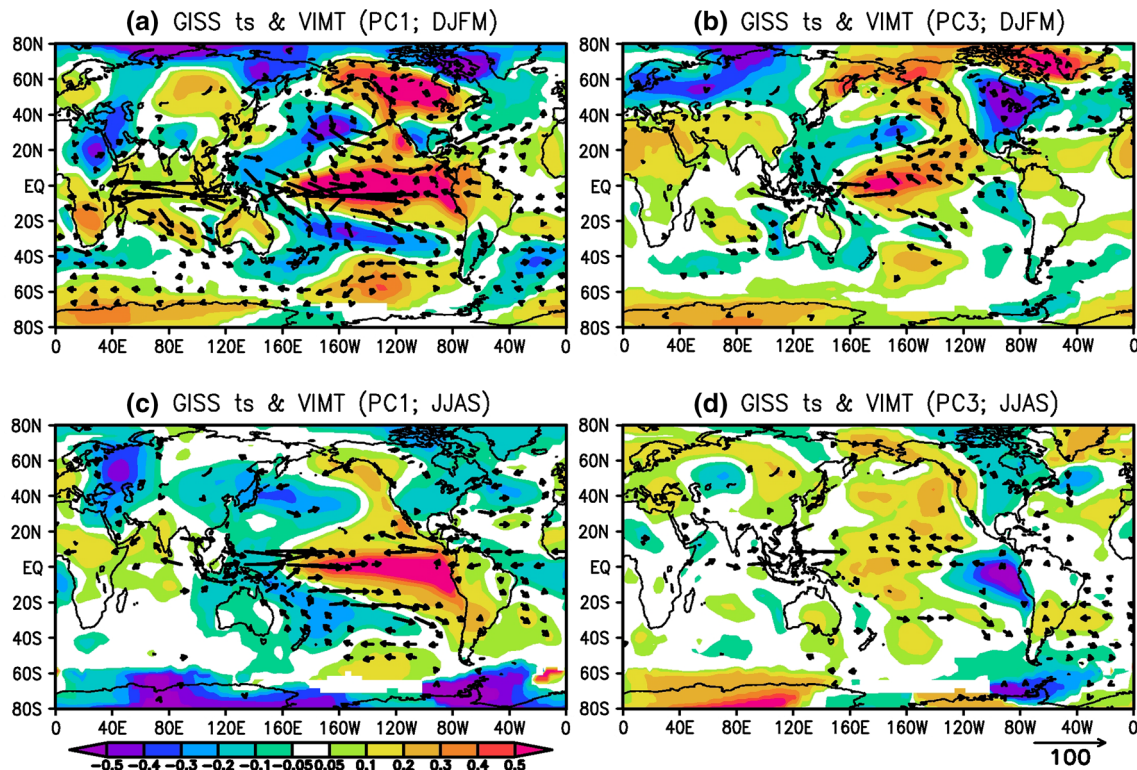


**Fig. 8** GISS ts anomalies (K; color shades) and VIMT ( $\text{kg m}^{-1} \text{s}^{-1}$ ; vectors; same as in Fig. 7) anomalies regressed onto the standardized PC1 (a, c) and PC3 (b, d) during DJFM (a, b) and JJAS (c, d),

respectively. VIMT vectors are shown only if at least one of their components is at the 90% significance level

become negligible during JJAS, while a cyclonic anomaly center is seen during DJFM with positive (negative) precipitation anomalies occurring in its southeastern (northwestern) portion. While surface temperature anomalies in the tropics tend to have similar spatial features during both seasons, which are also similar as the one derived for the whole year, seasonal differences are evident as well especially in the NH mid-high latitudes.

Responses of seasonal mean TMT and MERRA temperature anomalies at 500 hPa (T500) to the two ENSO flavors are also estimated. Since the anomalies associated with both ENSO flavors are generally weak during JJAS (not shown), anomaly patterns during DJFM are emphasized here (Fig. 9a–d). PC1 and PC3 related TMT anomalies during DJFM are generally consistent with the corresponding ones for full seasons (Fig. 3), respectively. Much more intense TMT anomalies are seen for PC1 than for PC3, especially in the tropics. Spatial structures of TMT anomalies are different between the two flavors not only in the tropics, and also in the subtropics/extratropics, specifically in the Northern Hemisphere. Spatial structures of MERRA T500 anomalies tend to be in agreement with corresponding anomaly features in TMT for both flavors. It is noted that zonal and interhemispheric symmetries can be seen in

temperature anomalies for PC1 as mentioned above, but are weak for PC3. PC3 tends to favor more intense temperature variations in the Northern Hemisphere.

Zonal wind anomalies at 250 hPa (U250) associated with PC1 and PC3 are further estimated (Fig. 9e, f). Differences in the spatial structures of U250 anomalies can readily be seen globally. For PC1, intense anomalies extend from the deep tropical zone into the mid-high latitudes of both hemispheres, manifesting evident teleconnection patterns (e.g., Trenberth et al. 1998). On the other hand, PC3's impact is relatively weaker and tends to be in the Northern Hemisphere. Zonal components of VIMT anomalies (UQv) for the two ENSO flavors are shown in Fig. 9g, h for comparison. Evident differences can be easily found not only in the deep tropics but also in the subtropics of both hemispheres.

It is further of interest to note that the PC3 related responses in several components during DJFM manifest an evident tri-polar structure in the North Atlantic basin as pointed out above. This tends to further confirm that the CP ENSO events might have a more organized effect on this region possibly by modulating NAO as proposed in previous studies (e.g., Brönnimann 2007; Graf and Zanchettin 2012). However, this tri-polar feature generally disappears during JJAS (not shown).

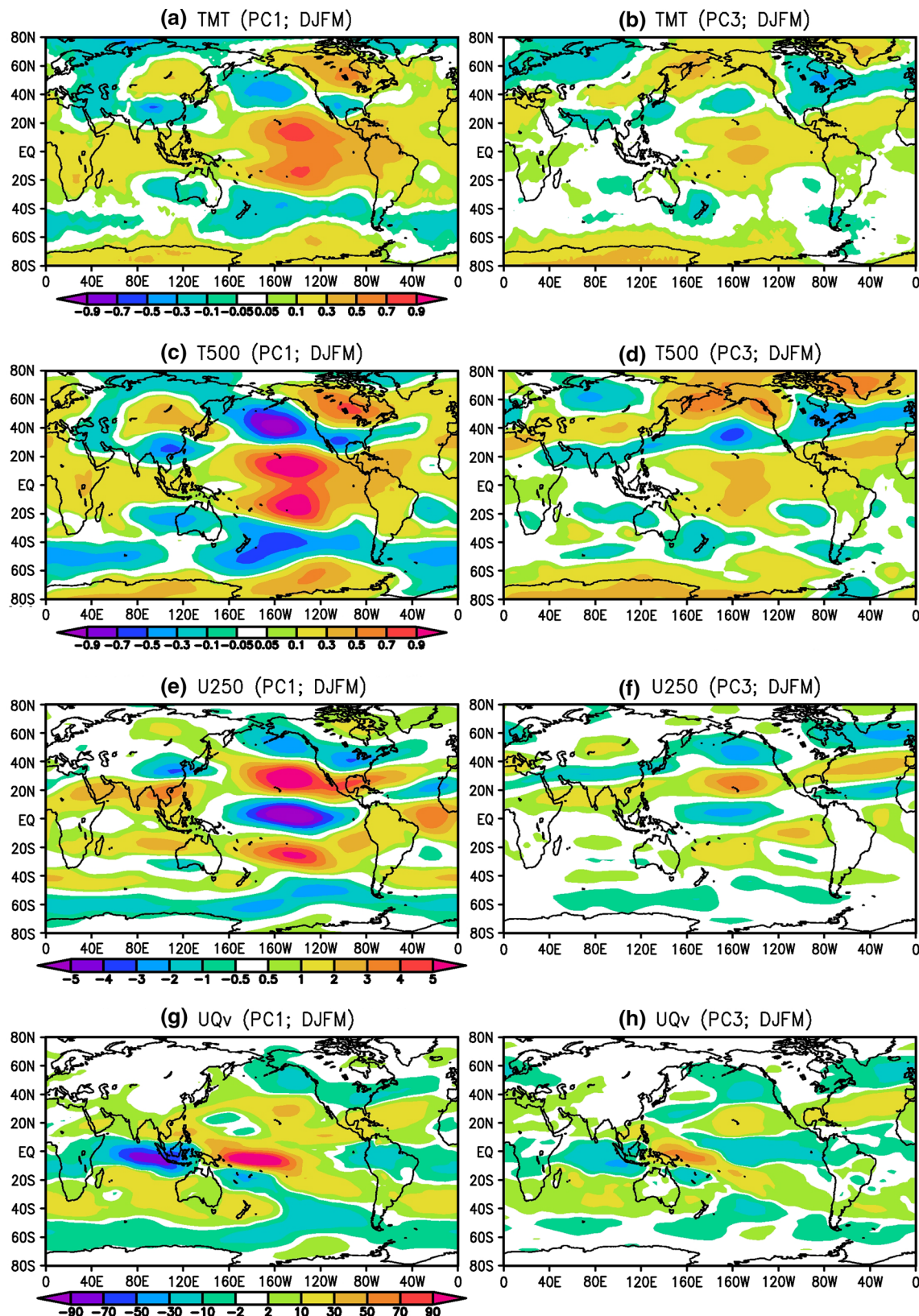
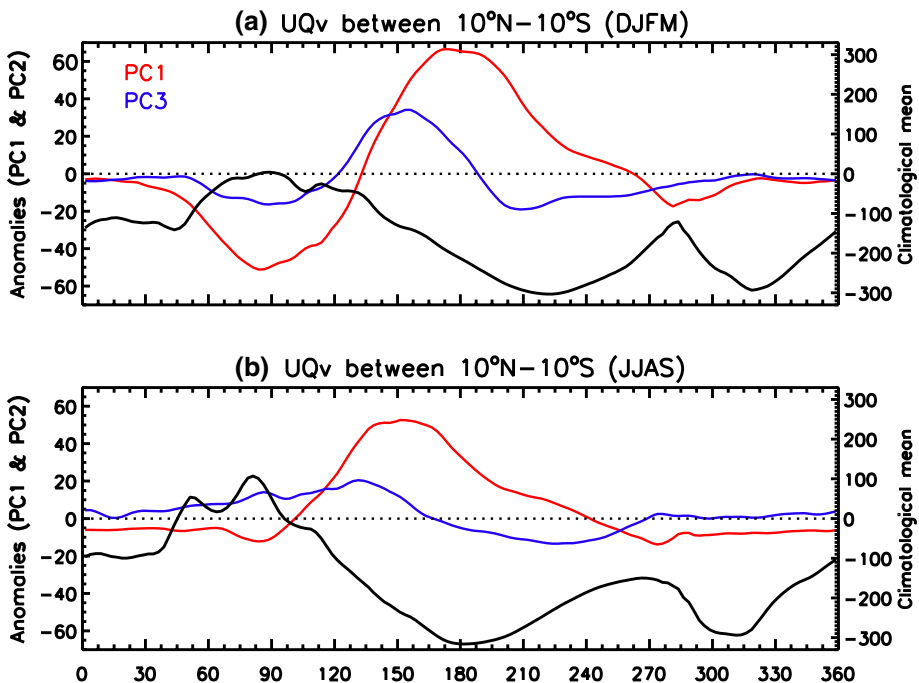


**Fig. 9** Regression maps of MSU/AMSU TMT (K; **a, b**), temperature at 500 hPa (K; **c, d**), zonal wind at 250 hPa ( $\text{m s}^{-1}$ ; **e, f**), and vertically integrated zonal moisture transport ( $\text{kg m}^{-1} \text{s}^{-1}$ ; **g, h**) onto the standardized PC1 (**a, c, e, g**) and PC3 (**b, d, f, h**) during DJFM

**Fig. 10** Vertically integrated zonal moisture transport anomalies ( $\text{kg m}^{-1} \text{s}^{-1}$ ) between  $10^\circ\text{N}$  and  $10^\circ\text{S}$  regressed onto the standardized PC1 (red) and PC3 (blue) during DJFM (a) and JJAS (b), respectively. Also shown are the corresponding climatological seasonal means (black;  $\text{kg m}^{-1} \text{s}^{-1}$ )



### 3.2.1 Zonal variations in the deep tropics

Spatial structures of atmospheric moisture transport represented by VIMT vector anomalies during the two contrasting seasons have been shown above for the two ENSO flavors (Figs. 7, 8). In this subsection, we further explore how atmospheric moisture transport in the deep tropics varies with the changes in the large-scale zonal circulation (i.e., the Pacific Walker Circulation) and divergent flows corresponding to the two ENSO flavors.

Zonal moisture transports in the deep tropics accompanying the two ENSO flavors are examined by regressing UQv anomalies between  $10^\circ\text{N}$  and  $10^\circ\text{S}$  against seasonal mean PC1 and PC3 (Fig. 10). Positive anomalies occur in the western-central Pacific for both flavors and during both seasons, confirming the eastward transport of atmospheric moisture during two distinct warm ENSO events, which is against the climatological mean state of zonal moisture transport in the tropical Pacific (black curves in Fig. 10). Positive UQv anomalies related to PC3 are generally weaker than the ones associated with PC1 during both seasons; and the peaks of positive UQv anomalies for PC3 are located west of the corresponding PC1 peaks. There are also strong seasonal variations in UQv anomalies for each ENSO flavor. More intense anomalies appear during DJFM in which most ENSO warm events reach their mature phase, and moreover the corresponding maximum peaks of positive anomalies specifically in the Pacific tend to be located east of their counterparts during JJAS, suggesting the seasonal shift in zonal moisture transport during the evolution of ENSO events.

The large-scale divergent flow patterns of total moisture transport are further examined by estimating the two ENSO flavors associated potential function ( $\varphi$ ) anomalies of VIMT during two seasons (Fig. 11), which can provide a description of how total atmospheric moisture is transported within the entire troposphere. Two centers of  $\varphi$  anomalies (one positive, another negative) are seen in the Pacific basin for PC1 during both seasons, while the centers during JJAS tend to shift to the west of their counterparts during DJFM. For PC3, the magnitudes of  $\varphi$  anomalies are much smaller. In particular, the PC3 related  $\varphi$  anomalies are very weak and are not organized very well during JJAS.

### 3.2.2 Zonal mean variability

Zonal mean profiles of GPCP precipitation anomalies regressed to PC1 and PC3 during DJFM and JJAS are depicted in Fig. 12a, b, respectively. During DJFM, positive precipitation anomalies occur along the equator with a peak just south of the equator for PC1 corresponding to the tropical dominance of positive precipitation anomalies in the central-eastern Pacific (Fig. 7a), while negative anomalies are in the subtropics with one peak around  $10^\circ\text{N}$  and another near  $20^\circ\text{S}$ . There is another positive peak around  $30^\circ\text{N}$ , mostly contributed by precipitation increases along the east coast of the Asian continent, over North Pacific, and in the North Atlantic basin (Fig. 7a). For PC3, a positive precipitation peak, albeit weaker than the equatorial maximum related to PC1, appears north of the equator, manifesting the northward shift of the eastern Pacific ITCZ (Fig. 7b). In the subtropics and extratropics, PC3 related

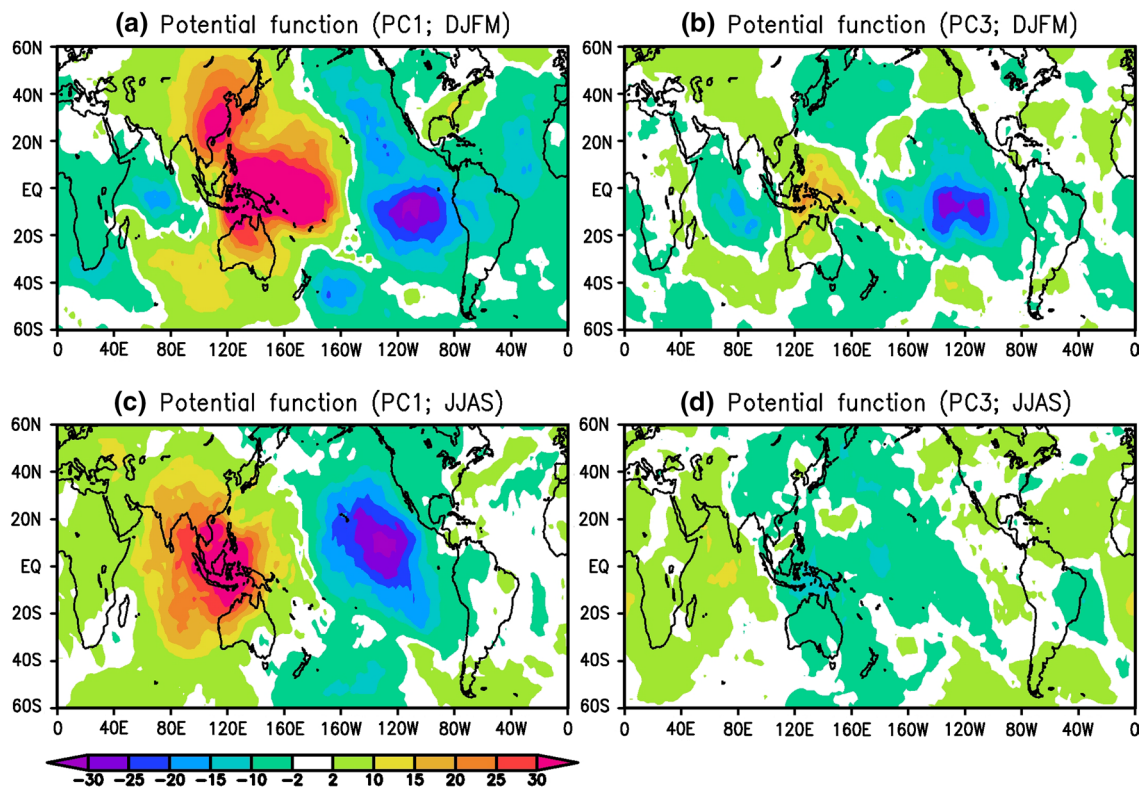


**Fig. 11** Potential function anomalies ( $10^6 \text{ kg s}^{-1}$ ) of VIMT regressed onto the standardized PC1 (a, c) and PC3 (b, d) during DJFM (a, b) and JJAS (c, d), respectively

zonal mean precipitation anomalies are in general weak (Fig. 7b), though precipitation decreases in the subtropics of both hemispheres and increases in the NH midlatitudes can still be discernible.

During JJAS, zonal mean precipitation anomalies are approximately comparable in magnitude between the two ENSO flavors (Fig. 12b). In particular, the PC1 related zonal mean anomalies become much weaker than during DJFM, and the equatorial maximum shifts north of the equator. For PC3, negative anomalies occupy the equatorial zone with a minimum peak just north of the equator, which pushes the positive peak northward to around 10°N.

Zonal mean profiles of MERRA precipitation anomalies are in general consistent with those derived from GPCP for both ENSO flavors especially during DJFM (Fig. 11c, d). During JJAS, for each ENSO flavor the corresponding positive peak in the tropics appears near the same latitude as the GPCP one, and their magnitudes are generally comparable. However, detailed discrepancies exist for both flavors. For PC1, much stronger negative precipitation anomalies in MERRA are seen in the both subtropics, though they are located roughly at the same latitudes as respective GPCP ones. For PC3, MERRA precipitation anomalies along the equator are positive compared to the negative anomaly zone in GPCP. There is also a positive peak near 40°S that is not

seen in GPCP. These differences suggest the limitations of MERRA precipitation specifically during boreal summer in which the warm events are relatively weak. Zonal mean moisture convergence anomalies from MERRA are further estimated corresponding to PC1 and PC3 during both seasons (Fig. 12e, f). Consistencies with both GPCP and MERRA precipitation can readily be found, especially regarding their respective peaks, roughly consistent with the spatial patterns of anomalies shown in Fig. 4. However, detailed differences between zonal mean precipitation and moisture convergence anomalies exist especially for PC1 related anomalies during DJFM, likely suggesting the contributions of surface evaporation (E).

To further understand the meridional distributions of precipitation anomalies due to these two ENSO flavors, their related zonal mean meridional moisture transports (VQv) are estimated (Fig. 13). Large differences exist between EP and CP events during both seasons. During DJFM (Fig. 13a), the climatological mean profile of VQv includes two opposite-sign zones: the first one is dominated by the southward transport extending from about 20°N to the SH mid-high latitudes with one peak near 10°N and another near 45°S, and the second one is located north of about 20°N in which the northward transport is dominant with a peak near 40°N. Both ENSO flavors can effectively

**Fig. 12** Zonal mean GPCP (**a**, **b**) and MERRA (**c**, **d**) precipitation anomalies ( $\text{mm day}^{-1}$ ), and convergence (**e**, **f**) anomalies ( $\text{mm day}^{-1}$ ) of VIMT regressed onto the standardized PC1 (black) and PC3 (red) during DJFM (**a**, **c**, **e**) and JJAS (**b**, **d**, **f**), respectively

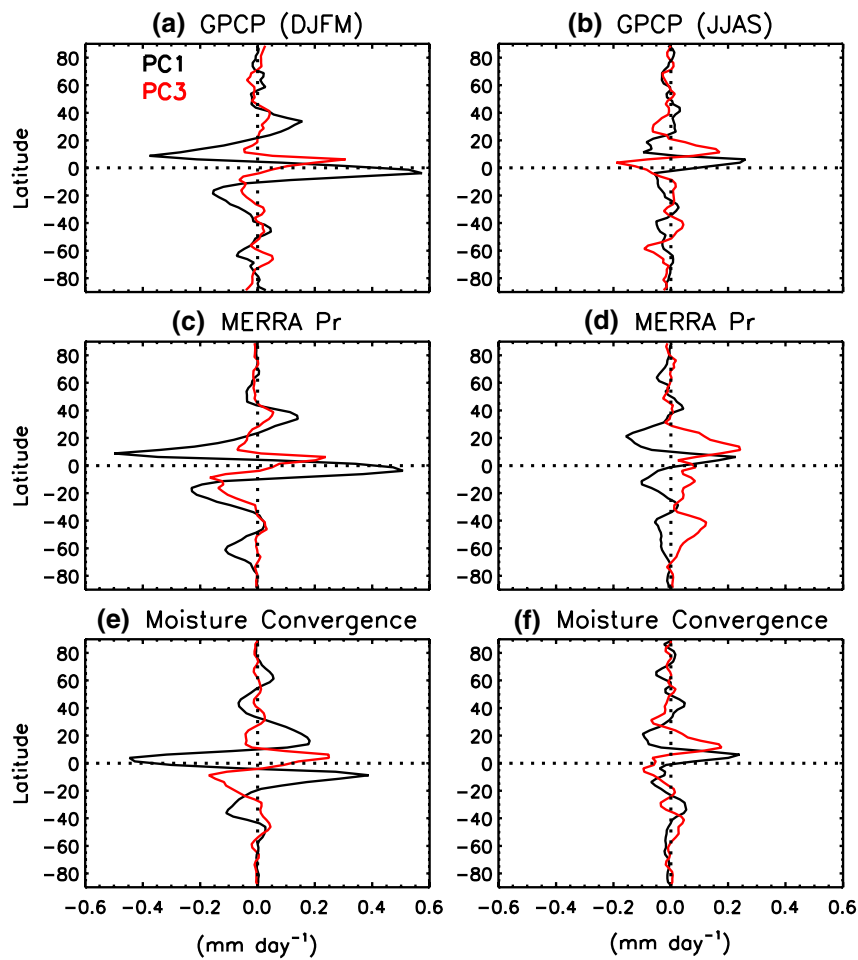
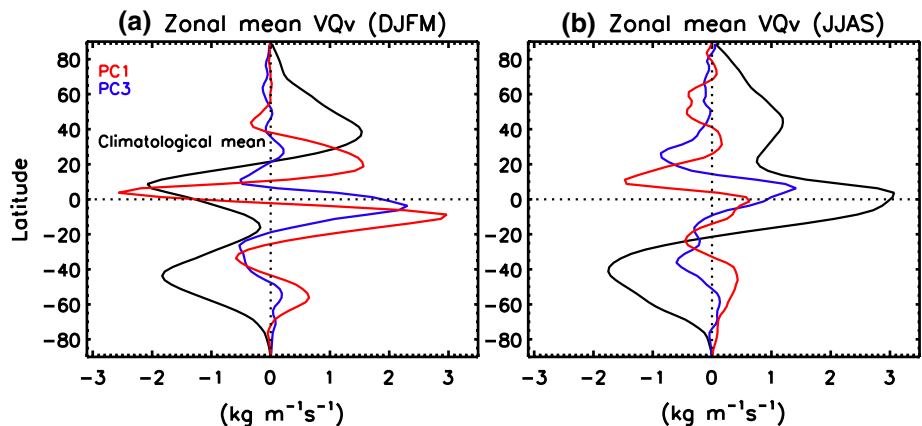


**Fig. 13** Zonal mean vertically integrated meridional moisture transport ( $\text{kg m}^{-1} \text{s}^{-1}$ ) regressed onto the standardized PC1 (red) and PC3 (blue) during DJFM (**a**) and JJAS (**b**), respectively. Also shown are the corresponding climatological zonal mean profiles (black; scaled by  $20 \text{ kg m}^{-1} \text{s}^{-1}$ )



modulate the climatological mean of meridional moisture transport likely through influencing the large-scale meridional circulation, i.e., the Hadley Cell (e.g., Oort and Yienger 1996; Trenberth et al. 1998). For PC1, southward moisture transport occurs between the equator and about  $10^{\circ}\text{N}$ , accompanied by northward transports within a broad

latitudinal band of  $10\text{--}40^{\circ}\text{N}$  and another latitudinal band south of the equator between about  $5\text{--}30^{\circ}\text{S}$ . For PC3, the effect is readily seen as well, with strong northward, cross-equatorial transports of moisture extending from  $20^{\circ}\text{S}$  to about  $10^{\circ}\text{N}$ , notwithstanding that the associated meridional features are totally different from those related to PC1.

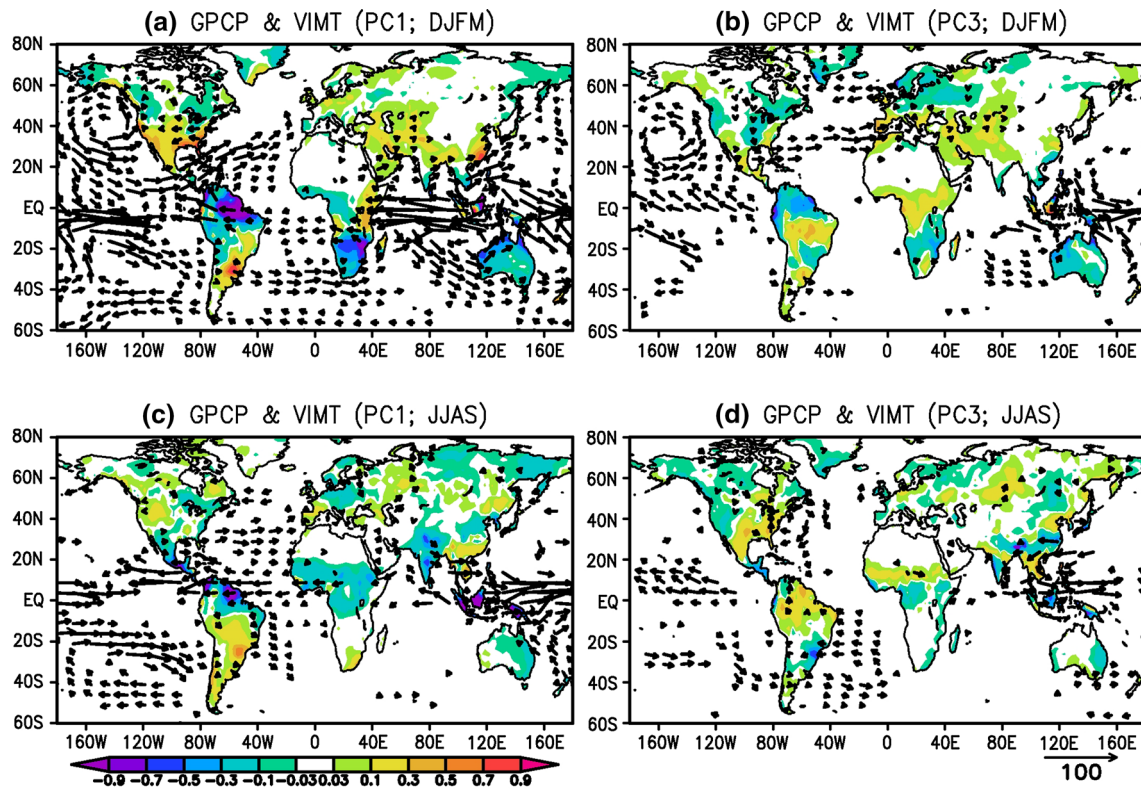


**Fig. 14** Regression maps of GPCP land precipitation anomalies ( $\text{mm day}^{-1}$ ; color shades) and VIMT ( $\text{kg m}^{-1} \text{s}^{-1}$ ; vectors) onto the standardized PC1 (a, c) and PC3 (b, d) during DJFM (a, b) and JJAS

(c, d). VIMT vectors are shown only if at least one of their components is at the 90% significance level

During JJAS (Fig. 13b), the climatological zonal profile of meridional moisture transport in the tropics tends to be opposite with that in boreal winter. Northward moisture transport dominates north of about  $20^{\circ}\text{S}$  with one large peak near the equator and another one close to  $40^{\circ}\text{N}$ . South of about  $20^{\circ}\text{S}$ , southward moisture transport prevails. Both ENSO flavors can modulate this climatological distribution, though their effects are relatively weaker than during DJFM. It is also readily found that their effects are different. PC1 induces southward transport between  $0$  and  $25^{\circ}\text{N}$  and enhances northward transport from the equator to about  $20^{\circ}\text{S}$ . PC1 related variations also exist in the subtropics and extratropics of both hemispheres. For PC3, enhanced northward transport occurs in the deep tropics: from about  $10^{\circ}\text{S}$ – $20^{\circ}\text{N}$ , while its related southward transport anomalies appear in the subtropics of both hemispheres:  $20$ – $40^{\circ}\text{N}$  and  $10$ – $50^{\circ}\text{S}$ .

### 3.2.3 Moisture transport and land precipitation

The large-scale features of precipitation and VIMT anomalies associated with the two ENSO flavors have been discussed above, including their respective seasonal variations

(Fig. 7). Since those features are primarily ocean-dominated, this subsection is focused on global land precipitation anomalies and possible connections with atmospheric moisture transport. Figure 14 is the same as Fig. 7, but PC1 and PC3 related seasonal mean GPCP precipitation anomalies are depicted here only over land (north of  $60^{\circ}\text{S}$ ) with different color scales to emphasize their spatial structures. Anomalies of VIMT convergence over land associated with the two ENSO flavors are also estimated during both seasons, which have roughly the same spatial distributions as respective precipitation anomalies (not shown), suggesting the dominance of tropospheric moisture transport in precipitation variations.

Large differences in precipitation anomalies can be observed between the two ENSO flavors (EP and CP events) over many land regions during two seasons. During DJFM, more intense precipitation anomalies across global lands are observed for PC1, accompanied by much more evident VIMT anomalies in the tropical and subtropical ocean basins (Fig. 14a, b). Over South America, both ENSO flavors (EP and CP events) induce negative precipitation anomalies over the deep tropical portion, with the effect from EP events being much stronger; and PC1

related precipitation anomalies are accompanied by significant westward moisture transport anomalies, which are not seen for PC3. Prominent precipitations anomalies occur also in the other parts of the continent for both flavors. However, spatial structures of precipitation anomalies tend to be different between the two flavors, with positive (negative) anomalies occurring in the southeastern (northwestern) portion for PC1 and a tri-polar structure of anomalies south of about 10°S for PC3. Also, significant VIMT anomalies can be found for PC1 south of about 20°S, but only a narrow band of VIMT anomalies appears roughly along 40°S for PC3.

Over North America, PC1 related negative precipitation anomalies are observed over two large areas north of about 40°N: one is near the west coast, another occupies the northeastern part of the continent. South of them, precipitation increases are seen, which correspond to the onshore moisture transport along both the west and east coast of North America. For PC3, negative precipitation anomalies occur along the west coast north of about 35°N and over a large area extending from the central-southern plains within the interior continent to the northeastern portion of the continent. Unlike PC1, precipitation anomalies over the southern portion of the continent are weak, though weak positive anomalies are still seen along the southeast coast, over the southwest domain, and in Central America. PC3 related onshore moisture transports are also weak.

In the African continent, PC1 related precipitation anomalies tend to be stronger than those for PC3. Although precipitation increase occurs for both flavors in the tropical East Africa, their effects in the tropical West Africa are opposite. Also, negative precipitation anomalies occur in the southern portion of the continent for both flavors, though PC3 has a weaker effect and its related anomalies is positive in the southeastern tip. It is also noted that the PC1 related VIMT anomalies accompanying precipitation anomalies can be observed specifically in the tropical East Africa and south of the equator, while no significant VIMT anomalies are seen for PC3.

Both PC1 and PC3 are related to significant northeastward moisture transport anomalies in North Atlantic, which might be the essential means for positive precipitation anomalies over West Europe and the Mediterranean basin. However, differences in their effects can be readily found. PC1 related precipitation anomalies in these regions are generally weak, while PC3 can induce much stronger precipitation increase within the Mediterranean basin and cause precipitation decrease over most of West Europe, forming a north–south dipolar structure of precipitation anomalies. Also, the south (north) pole is clearly followed by significant onshore (offshore) moisture transport. Furthermore, the PC3 related onshore moisture transport through the Mediterranean basin might be able

to penetrate deeper into the interior Eurasia where precipitation increases are observed. PC1 related precipitation increase could also be seen roughly over the same region. Nevertheless, significant moisture transport seems to come from the south, which might be partly connected with the variations in the Asian monsoon. Therefore, the CP type events (PC3) tend to have more systematic impact on West Europe and the Mediterranean basin, and the dipolar structure of precipitation anomalies and associated moisture transport anomalies in North Atlantic further confirm that stronger ENSO modulation of NAO might happen during the occurrence of CP events (e.g., Graf and Zanchettin 2012).

In the East Asian region, PC1 is related to strong precipitation increase, concurrent with anomalous southwesterly moisture transport, confirming the effect of the canonical warm ENSO events discovered in previous studies (e.g., Wang et al. 2000; Weng et al. 2009). PC3's effect can also be observed, albeit weak, through forming a north–south dipolar distribution of precipitation anomalies (e.g., Zhang et al. 2014), even though no significant moisture transport anomalies appear.

Negative precipitation anomalies occur over Australia for both ENSO flavors, although PC1 tends to have much stronger impact than PC3. Also, systematic and significant VIMT anomalies are observed for PC1, but moisture transport anomalies are in general weaker for PC3.

Seasonal differences in the impact of the two ENSO flavors are evident, including both their related, respective precipitation anomalies and corresponding VIMT anomalies. During JJAS (Fig. 14c, d), PC1 corresponds to negative precipitation anomalies in the deep tropical portion of South America, along with significant westward VIMT anomalies, and positive precipitation anomalies cover most of the continent in the Southern Hemisphere. For PC3, however positive precipitation anomalies occupy most of tropical South America during JJAS, and weak negative precipitation anomalies are observed over a small region near the northern tip of the continent and in the southeastern zone. Over North America, a dipolar pattern of precipitation anomalies is associated with PC1 roughly along 20–50°N over the west half of the continent, accompanied by weak VIMT anomalies; For PC3, a dipolar structure of precipitation anomalies is also seen, but with negative anomalies occupying the northwestern portion and positive ones over the southeastern part of the continent. Over West Africa, the effects are generally opposite between the two flavors, with PC1 being related to negative anomalies and PC3 to positive ones. PC1 can also have influence on regions over the Eurasian continent during JJAS. For instance, weak negative precipitation anomalies over West Europe and NH high latitudes roughly extending from 80°E to east Siberia; Negative precipitation anomalies also

appear in the Indian monsoon region, and a dipolar pattern of anomalies in the East Asia. Scattered precipitation anomalies occur in the Eurasia for PC3 as well, but both precipitation and VIMT anomalies in general are not organized as coherently as during DJFM. However, PC3 seems to have stronger impact in the southeast and East Asia than during DJFM, with regard to both precipitation and VIMT anomalies (Fig. 14b, d).

#### 4 Summary and concluding remarks

The effects of two ENSO flavors, i.e., the EP and CP events, on global temperature, precipitation, and atmospheric moisture transport during 1979–2014 are examined by means of satellite-/ground-based observations and the NASA MERRA reanalysis product. The first and third modes from an EOF analysis of monthly SST anomalies between 30°N and 30°S are found to represent very well the EP and CP ENSO events, respectively. The corresponding principal components are then used as indices in estimating their impact on a variety of physical components. The two ENSO flavors have distinct SST configurations in the tropical Pacific, hence manifesting different spatial patterns of precipitation anomalies in the global tropics and the mid-high latitudes of both hemispheres. Large differences also exist between them in the variations in surface and tropospheric temperature, columnar water vapor content, and vertically integrated moisture transport, suggesting their distinct means of influencing precipitation and hydrological cycle components across the world.

Their effects during two contrasting seasons, boreal winter (DJFM) and summer (JJAS), are further explored. Zonal moisture transport anomalies in the deep tropics following the variations in the Pacific Walker Circulation are distinctly different between the two ENSO flavors during both seasons. For each flavor, associated precipitation and VIMT anomalies also manifest evident seasonal variations. In general, more intense anomalies appear during DJFM in which ENSO warm events usually reach their mature phase, and the corresponding maximum peaks of positive anomalies for both precipitation and zonal component of total moisture transport (UQv) specifically in the Pacific tend to be located east of their counterparts during JJAS. Estimated potential function ( $\varphi$ ) anomalies of VIMT corresponding to these two ENSO flavors also have strong seasonality, and the differences between them are evident with regard to the locations of respective positive/negative  $\varphi$  centers and strength.

Zonal mean precipitation anomalies from both GPCP and MERRA have different meridional features as well for the two ENSO flavors during two seasons, which are accompanied by evident differences in respective zonal

mean VIMT (both zonal and meridional components) anomalies. Tropical peaks of precipitation anomalies are different for the two flavors regarding both preferred latitudinal location and magnitude. Differences in vertically integrated moisture convergence, and cross-equatorial and poleward moisture transport denoted by zonal mean VQv anomalies are also evident. Again, for each flavor, its effect has strong seasonality.

It is further noted that the two ENSO flavors are associated with distinct precipitation anomaly patterns over various global land regions particularly during DJFM when the warm ENSO events usually reach their mature phase, which are also closely related to the differences in VIMT anomalies. For instance, during DJFM the EP events in general have much stronger impact in the East Asia and North America, while the CP events tend to have a more systematic influence in West Europe and the Mediterranean basin.

Finally, general agreements between observations and MERRA outputs including temperature, precipitation, and water vapor content exist, gauged by consistent spatial patterns of regressed anomalies corresponding to the two respective ENSO flavors. These agreements support the notion that MERRA outputs could provide an excellent measure of interannual variations in these hydrological-cycle components.

**Acknowledgements** The NASA-GISS global surface temperature anomaly product was downloaded from its website at <http://data.giss.nasa.gov/>. The ERSST data set (v4) was downloaded from the NOAA-NCDC website at <http://www.ncdc.noaa.gov/ersst/>. This research is supported under the NASA Modeling, Analysis, and Prediction (MAP) Program and the NASA Energy and Water-cycle Study (NEWS).

**Funding** Funding was provided by NASA MAP and NEWS Programs (Grant Nos. NNX13AN40G, NNX15AE45G).

#### References

- Adler RF, Huffman GJ, Chang A, Ferraro R, Xie P, Janowiak J, Rudolf B, Schneider U, Curtis S, Bolvin D, Gruber A, Susskind J, Arkin P (2003) The version 2 Global Precipitation Climatology Project (GPCP) monthly precipitation analysis (1979–present). *J Hydrometeorol* 4:1147–1167
- Ashok K, Behera SK, Rao SA, Weng H, Yamagata T (2007) El Niño Modoki and its possible teleconnection. *J Geophys Res* 112:C11007. doi:[10.1029/2006JC003798](https://doi.org/10.1029/2006JC003798)
- Brönnimann S (2007) Impact of El Niño-southern oscillation on European climate. *Rev Geophys* 45:RG3003. doi:[10.1029/2006RG000199](https://doi.org/10.1029/2006RG000199)
- Burgman RJ, Clement AC, Mitas CM, Chen J, Esslinger K (2008) Evidence for atmospheric variability over the Pacific on decadal time-scales. *Geophys Res Lett* 35:L01704. doi:[10.1029/2007GL031830](https://doi.org/10.1029/2007GL031830)
- Capotondi AC et al (2015) Understanding ENSO diversity. *Bull Am Meteorol Soc* 96:921–938. doi:[10.1175/BAMS-D-13-00117.1](https://doi.org/10.1175/BAMS-D-13-00117.1)
- Curtis S, Adler RF (2003) Evolution of El Niño-precipitation relationships from satellites and gauges. *J Geophys Res* 108(D4):4153. doi:[10.1029/2002JD002690](https://doi.org/10.1029/2002JD002690)

- Dai A, Wigley TML (2000) Global patterns of ENSO-induced precipitation. *Geophys Res Lett* 27:1283–1286
- Graf H-F, Zanchettin D (2012) Central Pacific El Niño, the “subtropical bridge”, and Eurasian climate. *J Geophys Res* 117:D01102. doi:[10.1029/2011JD016493](https://doi.org/10.1029/2011JD016493)
- Gu G, Adler RF (2013) Interdecadal variability/long-term changes in global precipitation patterns during the past three decades: global warming and/or Pacific Decadal Variability? *Clim Dyn* 40:3009–3022. doi:[10.1007/s00382-012-1443-8](https://doi.org/10.1007/s00382-012-1443-8)
- Gu G, Adler RF, Huffman GJ (2016) Long-term changes/trends in surface temperature and precipitation during the satellite era (1979–2012). *Clim Dyn* 46:1091–1105. doi:[10.1007/s00382-015-2634-x](https://doi.org/10.1007/s00382-015-2634-x)
- Hansen J, Ruedy R, Glascoe J, Sato M (1999) GISS analysis of surface temperature change. *J Geophys Res* 104:30997–31022
- Hong C-C, Li Y-H, Li T, Lee M-Y (2011) Impacts of central Pacific and eastern Pacific El Niños on tropical cyclone tracks over the western North Pacific. *Geophys Res Lett* 38:L16712. doi:[10.1029/2011GL048821](https://doi.org/10.1029/2011GL048821)
- Huffman GJ, Adler RF, Bolvin DT, Gu G (2009) Improvements in the GPCC global precipitation record: GPCC Version 2.1. *Geophys Res Lett* 36:L17808. doi:[10.1029/2009GL040000](https://doi.org/10.1029/2009GL040000)
- Kao H-Y, Yu J-Y (2009) Contrasting Eastern-Pacific and Central-Pacific types of ENSO. *J Clim* 22:615–632
- Kiladis GN, Diaz HF (1989) Global climatic anomalies associated with extremes in the Southern Oscillation. *J Clim* 2:1069–1090
- Kim H-M, Webster PJ, Curry JA (2011) Modulation of North Pacific tropical cyclone activity by three phases of ENSO. *J Clim* 24:1839–1849
- Kug J-S, Jin F-F, An S-I (2009) Two types of El Niño events: cold tongue El Niño and warm pool El Niño. *J Clim* 22:1499–1515
- Larkin NK, Harrison DE (2005) Global seasonal temperature and precipitation anomalies during El Niño autumn and winter. *Geophys Res Lett* 32:L16705. doi:[10.1029/2005GL022860](https://doi.org/10.1029/2005GL022860)
- Mayer M, Trenberth KE, Haimberger L, Fasullo JT (2013) The response of tropical atmospheric energy budget to ENSO. *J Clim* 26:4710–4724
- North GR, Bell TL, Cahalan RF, Moeng FJ (1982) Sampling error in the estimation of empirical orthogonal functions. *Mon Weather Rev* 110:699–706
- Oort AH, Yienger JJ (1996) Observed interannual variability in the hadley circulation and its connection to ENSO. *J Clim* 9:2751–2767
- Rienecker MM et al (2011) MERRA: NASA's modern-era retrospective analysis for research and applications. *J Clim* 24:3624–3648
- Robertson FR, Bosilovich MG, Chen J, Miller TL (2011) The effects of satellite observing system changes on MERRA water and energy fluxes. *J Clim* 24:5197–5217
- Robertson FR, Bosilovich MG, Roberts JB, Reichle RH, Adler R, Ricciardull L, Berg W, Huffman GJ (2014) Consistency of estimated global water cycle variations over the satellite era. *J Clim* 27:6135–6151
- Robinson WA (2002) On the midlatitude thermal response to tropical warmth. *Geophys Res Lett* 29:1190. doi:[10.1029/2001GL014158](https://doi.org/10.1029/2001GL014158)
- Ropelewski CF, Halpert MS (1987) Global and regional scale precipitation patterns associated with the El Niño/Southern Oscillation. *Mon Weather Rev* 115:1606–1626
- Seager R, Harnik N, Kushnir Y, Robinson WA, Miller J (2003) Mechanisms of hemispherically symmetric climate variability. *J Clim* 16:2960–2978
- Smith TM, Reynolds RW, Peterson TC, Lawrimore J (2008) Improvements to NOAA's historical merged land–ocean surface temperature analysis (1880–2006). *J Clim* 21:2283–2296
- Sohn B-J, Smith EA, Robertson FR, Park S-C (2004) Derived over-ocean water vapor transports from satellite-retrieved E–P datasets. *J Clim* 17:1352–1365
- Takahashi K, Montecinos A, Goubanova K, Dewitte B (2011) ENSO regimes: reinterpreting the canonical and Modoki El Niño. *Geophys Res Lett* 38:L10704. doi:[10.1029/2011GL047364](https://doi.org/10.1029/2011GL047364)
- Trenberth KE, Stepaniak DP (2001) Indices of El Niño evolution. *J Clim* 14:1697–1701
- Trenberth KE, Smith L (2009) Variations in the three-dimensional structure of the atmospheric circulation with different flavors of El Niño. *J Clim* 22:2978–2991
- Trenberth KE, Fasullo JT (2013) An apparent hiatus in global warming? *Earth's Future*. doi:[10.1002/2013EF000165](https://doi.org/10.1002/2013EF000165)
- Trenberth KE, Branstator GW, Karoly D, Kumar A, Lau N-C, Ropelewski C (1998) Progress during TOGA in understanding and modeling global teleconnections associated with tropical sea surface temperatures. *J Geophys Res* 103:14291–14324
- Trenberth KE, Fasullo JT, Mackaro J (2011) Atmospheric moisture transport from ocean to land and global energy flows in reanalysis. *J Clim* 24:4907–4924
- Wang B, Wu R, Fu X (2000) Pacific-East Asia teleconnection: how does ENSO affect East Asian climate? *J Clim* 13:1517–1531
- Weng H, Ashok K, Behera SK, Rao SA, Yamagata T (2007) Impacts of recent El Niño Modoki on dry/wet conditions in the Pacific Rim during boreal summer. *Clim Dyn* 29:113–129
- Weng H, Behera SK, Yamagata T (2009) Anomalous winter climate conditions in the Pacific rim during recent El Niño Modoki and El Niño events. *Clim Dyn* 32:663–674
- Wentz FJ (1997) A well-calibrated ocean algorithm for special sensor microwave/imager. *J Geophys Res* 102(C4):8703–8718
- Xue Y, Smith TM, Reynolds RW (2003) Interdecadal changes of 30-yr SST normals during 1871–2000. *J Clim* 16:1601–1612
- Yulaeva E, Wallace JM (1994) The signature of ENSO in global temperature and precipitation fields derived from the Microwave Sounding Unit. *J Clim* 7:1719–1736
- Zhang Y, Wallace JM, Battisti DS (1997) ENSO-like interdecadal variability: 1900–93. *J Clim* 10:1004–1020
- Zhang W, Jin F-F, Turner A (2014) Increasing autumn drought over southern China associated with ENSO regime shift. *Geophys Res Lett* 41:4020–4026. doi:[10.1002/2014GL060130](https://doi.org/10.1002/2014GL060130)